

Mid-IR focal plane array based on type-II InAs/GaSb strain layer superlattice detector with nBn design

H. S. Kim,¹ E. Plis,¹ J. B. Rodriguez,^{1,a)} G. D. Bishop,¹ Y. D. Sharma,¹ L. R. Dawson,¹ S. Krishna,^{1,b)} J. Bundas,² R. Cook,² D. Burrows,² R. Dennis,² K. Patnaude,² A. Reisinger,² and M. Sundaram²

¹Center for High Technology Materials, Department of Electrical and Computer Engineering, University of New Mexico, Albuquerque, New Mexico 87106, USA

²QmagiQ, LLC, One Tara Boulevard, Suite 102, Nashua, New Hampshire 03062, USA

(Received 7 February 2008; accepted 16 April 2008; published online 7 May 2008)

A midwave infrared camera ($\lambda_c=4.2\ \mu\text{m}$) with a 320×256 focal plane array (FPA) based on type-II InAs/GaSb strain layer superlattice (SLs) has been demonstrated. The detectors consist of an nBn heterostructure, wherein the SL absorber and contact layers are separated by a $\text{Al}_{0.2}\text{Ga}_{0.8}\text{Sb}$ barrier layer, which is designed to have a minimum valence band offset. Unlike a PN junction, the size of the device is not defined by a mesa etch but confined by the lateral diffusion length of minority carriers. At 77 K, the FPA demonstrates a temporal noise equivalent temperature difference (NETD) of 23.8 mK ($T_{\text{int}}=16.3\ \text{ms}$ and $V_b=0.7\ \text{V}$) with a peak quantum efficiency and detectivity at $3.8\ \mu\text{m}$ equal to 52% and 6.7×10^{11} Jones, respectively. © 2008 American Institute of Physics.

[DOI: 10.1063/1.2920764]

Midwave-infrared (MWIR) focal plane arrays (FPAs) are widely used for a variety of imaging applications, including medical diagnostics and terrestrial surveillance. State-of-the-art detectors are based on interband transitions in PN junctions made from either InSb or HgCdTe (MCT) or on intersubband transitions in quantum well IR (QWIP) detectors. However, lack of spatial uniformity over a large area still plagues InSb and MCT devices, while QWIPs have larger dark currents and lower quantum efficiency (QE) compared to the interband devices. Type-II InAs/GaSb superlattices (SLs) for IR detection were first proposed by Smith and Mailliot in 1987.¹ Since then, SL based detectors have been considered as an alternative technology for the fabrication of high performance FPAs. The effective band gap of the InAs/InGaSb SLs can be tailored from 3 to $30\ \mu\text{m}$ by varying thickness of constituent layers thus allowing fabrication of devices with operating wavelengths spanning the entire IR region. Moreover, normal incidence absorption is permitted in these structures resulting in high QE. Commercial availability of low defect density substrates and a high degree of uniformity for III-V processing over a large area also offers technological advantages for the SLs. In addition, detector performance at high temperature is expected to be improved because of a comparatively large effective electron mass ($\sim 0.04m_0$) that enables SLs to suppress tunneling effect, and Auger recombination processes.² This makes SLs an attractive technology for realization of high performance third generation FPAs.

Presently, all SL detectors are based on a photodiode design. In this case, the optically active area of the photodiode is defined by an etched mesa. During the mesa isolation process, the periodic nature of the idealized crystal structure abruptly ends at the mesa lateral surface. Disturbance of the periodic potential function due to a broken crystal lattice

leads to allowed electronic quantum states within the energy band gap of SLs resulting in large surface leakage currents. The suppression of these currents is the most demanding challenge for present day SL technology, especially for long wavelength IR and very long wavelength IR spectral regions, since the dimensions of SL pixels have to be scaled to $\sim 20\ \mu\text{m}$ in FPAs. In order to overcome the limitation imposed by surface leakage currents, a stable surface passivation layer is needed. So far, various approaches have been proposed such as the deposition of polyimide layer,³ overgrowth of wide band gap material,⁴ deposition of passivating sulfur coating electrochemically,⁵ and post-etch treatment in chemical solutions.⁶ However, these passivation methods are either sensitive to the cutoff wavelength of the device or complicates the fabrication process of FPAs.

Recently, a nBn structure has been proposed to effectively suppress the surface leakage current and increase the operating temperature of InAs based detectors.⁷ The nBn detector with InAs and InAsSb materials have shown that the background limited IR photodetection temperature can be increased by 100 K. The nBn structure is composed of an n -type narrow band gap absorber layer with a wide band gap undoped barrier layer which is chosen to have a minimal valence band offset. This is then sandwiched between the top and bottom contacts. The band structure of the nBn design is shown in Fig. 1(a). The majority carrier (electron) current is blocked by a large conduction band offset whereas minority carriers (holes) freely move between the electrodes. Hence, the optically active area of nBn detector is defined by the diffusion length of minority carriers and not by the dimensions of the etched mesa. It is important to note that there is no surface leakage current in these devices since the individual pixels are not separated by an etched mesa. Recently, single pixel detectors based on the nBn structure with InAs/GaSb SLs as the n -type narrow band gap layer and an AlGaSb barrier layer have been reported.⁸⁻¹⁰ In this paper, we report on the fabrication of a 320×256 FPA based on this design with a cutoff wavelength of $4.2\ \mu\text{m}$ operating at 77 K.

^{a)}Present address: Institut d'Electronique du Sud (IES), UMR CNRS 5214, cc 067, Université Montpellier 2, 34095 Montpellier Cedex 05, France.

^{b)}Electronic mail: skrishna@chtm.unm.edu.

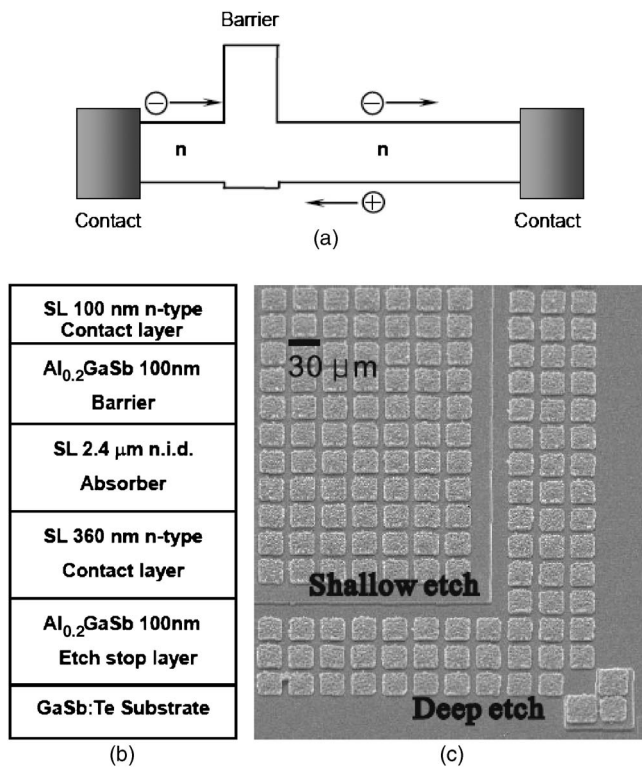


FIG. 1. (a) Band structure schematic of an nBn structure under applied bias. (b) The heterostructure schematic of nBn device. (c) SEM image showing part of fully processed FPA with deposited indium bumps. The two-step etch process is illustrated.

Detector samples were grown on Te-doped epitaxial (100) GaSb substrates using a solid source molecular beam epitaxy VG-80 system. The system was equipped with SUMO® cells for gallium and indium and a standard effusion cell for aluminum and cracker cells for antimony and arsenic. The growth details were reported elsewhere.¹¹ The detector structure consists of nominally undoped 100 nm thick Al_{0.2}Ga_{0.8}Sb etch stop layer followed by a 360 nm bottom contact layer formed by 8 ML InAs:Si ($n=4 \times 10^{18} \text{ cm}^{-3}$)/8 ML GaSb SLs. Then a 2.4 μm thick nonintentionally doped absorber formed by 8 ML InAs/8 ML GaSb SLs were grown followed by a 100 nm thick Al_{0.2}GaSb barrier layer. The SL absorption region is residual n -type with a carrier concentration in the low 10^{16} cm^{-3} at room temperature.¹² The structure was terminated by a

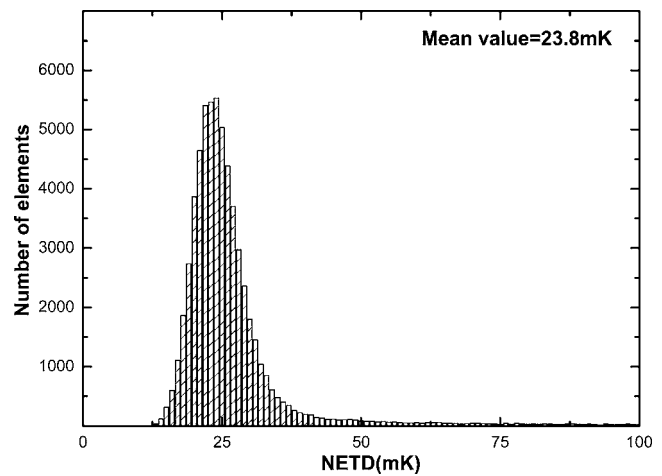


FIG. 2. Histogram of the NETD distribution in the FPA for an integration time of 16.3 ms with $f/2.3$ optics.

100 nm n -type ($n=4 \times 10^{18} \text{ cm}^{-3}$) top contact layer. The heterostructure schematic is presented in the Fig. 1(b).

Each processed FPA die consists of 320×256 pixels with a 30 μm pitch. On a quarter of a 2 in. GaSb wafer two FPAs were realized, each with an area of $10.34 \times 8.97 \text{ mm}^2$. Processing was initiated by defining $24 \times 24 \mu\text{m}^2$ squares with standard UV photolithography and a shallow wet chemical etch using phosphoric acid was performed. It is to be noted that the depth of the shallow etch was equal to 0.15 nm, which corresponds to the middle of the barrier layer. Thus, the active absorber layer underneath is untouched. Then an inductively coupled plasma dry etch to the middle of the bottom contact layer on the three outermost rows and columns of the FPA was undertaken. A scanning electron microscope (SEM) image of a part of a fully processed FPA is shown in the Fig. 1(c) and illustrates the two steps of the etching process. Top and bottom contacts were then deposited using an electron beam metal evaporation system. We used Ti/Pt/Au (500/500/3000 Å) as contact metals for both top and bottom Ohmic contact metallization. Finally, to enable well defined indium bumps, an under bump metal (UBM) deposition was conducted using Ti/Ni/Au (300/1500/500 Å). Indium bumps with a thickness $\sim 3 \mu\text{m}$ were thermally evaporated on UBM metal pads. Following this, the FPAs were hybridized to ISCO209 read-out integrated circuits (ROICs) made by Indigo.

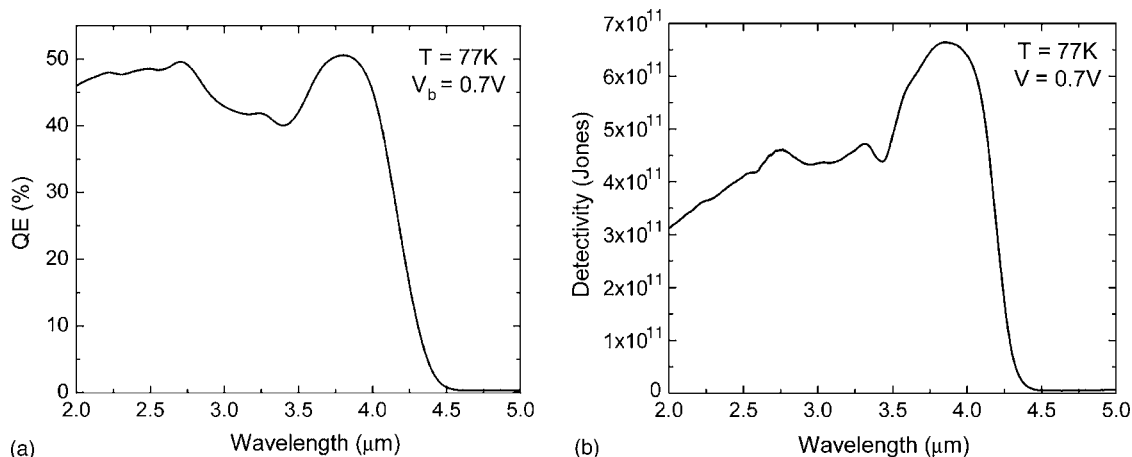


FIG. 3. (a) External QE and (b) peak detectivity at $V_b=0.7 \text{ V}$ for the 320×256 FPA.



FIG. 4. Thermal image taken with 320×256 InAs/GaSb SL *nBn* camera at a detector temperature of 77 K and integration time of 16.3 ms. Two-point NUC was utilized.

To reduce the free carrier absorption in the substrate and to minimize the thermal stress between the FPA and the ROIC under cool-down conditions, the substrate was completely removed from backside of the FPAs by a combination of mechanical polishing and wet chemical etching. Hybridization and characterization of the FPAs were undertaken at QmagiQ, LLC. Hybrid FPAs were tested on a CamIRa IR FPA evaluation system made by SE-IR Corporation with a Ge window for the imaging performance tests. For the tests, the background was a 300 K scene under $f/2.3$ illumination. The applied bias was equal to 0.7 V and is defined as a positive voltage applied to the bottom contact of the FPA.

The noise equivalent temperature difference (NETD) was measured by acquiring a sequence of 25 image scans with the focal plane exposed to a uniform blackbody target at 30 °C and extracting the temporal noise for each pixel. A histogram of the NETD distribution is shown in Fig. 2 for an integration time of 16.3 ms. Good spatial uniformity is obtained over the array, resulting in a median NETD value of 23.8 mK with a standard deviation of 10 mK at a FPA temperature of 77 K. Pixel operability was equal to 79% with predominant single pixel faults without large clusters. Pixel outages probably originated from the weak connection between the ROIC and FPA since the thickness of indium bumps was equal only 3 μm and no reflow process was utilized. Average dark current density of FPA was as low as 1×10^{-7} A/cm² at 77 K ($V_b=0.7$ V). This value is comparable to the state-of-the-art reports for MWIR detectors based on a conventional photodiode design with a passivation scheme.

External QE of FPA was obtained using the spectral response curve from the test diode on the FPA chip with $380 \times 380 \mu\text{m}^2$ optical area. Spectral measurements were performed using a Fourier transform IR spectrometer (FTIR). Under 0.7 V bias and at 77 K, the FPA exhibits a QE as high as 52% at 3.8 μm [Fig. 3(a)]. Peak responsivity and detectivity of FPA were estimated, respectively, to 1.6 A/W and 6.7×10^{11} Jones at 3.8 μm and 77 K ($V_b=0.7$ V). Values of specific detectivity as a function of wavelength are presented on the Fig. 3(b).

A thermal image taken with 320×256 MWIR FPA camera based on InAs/GaSb SLs at a detector temperature of 77 K and an integration time of 16.3 ms is shown in Fig. 4. Two point nonuniformity correction (NUC) was used for the imaging. Temperatures of 20 and 40 °C were utilized as the low and high temperature for the NUC correction algorithm. The bright areas of the image represent warmer regions whereas the dark areas exhibit colder regions. In the figure, the thermal imprint of the cold can is clearly visible demonstrating the good imaging quality of thermal imager.

In conclusion, we demonstrated 320×256 FPA based on type II InAs/GaSb SLs with *nBn* detector design. Average value of dark current density (1×10^{-7} A/cm² at 77 K ($V_b=0.7$ V)) is comparable to that reported for the state-of-the-art MWIR SL photodiodes utilizing some passivation schemes. At 77 K, FPA reveals a cutoff wavelength of 4.2 μm and NETD of 23.8 mK for 16.3 ms integration time. Peak responsivity and detectivity of FPA were estimated, respectively, to 1.6 A/W and 6.7×10^{11} Jones at 3.8 μm and 77 K.

The authors would like to acknowledge the support by AFRL Grant FA9453-07-C-0171 and HOT MWIR program.

¹D. L. Smith and C. Mailhot, *J. Appl. Phys.* **62**, 2545 (1987).

²M. Razeghi, H. Mohseni, and V. I. Litvinov, *Phys. Rev. B* **58**, 15378 (1998).

³A. Hood, P.-Y. Delaunay, D. Hoffman, B.-M. Nguyen, Y. Wei, and M. Razeghi, *Appl. Phys. Lett.* **90**, 233513 (2007).

⁴R. Rehm, M. Walther, F. Fuchs, J. Schmitz, and J. Fleissner, *Appl. Phys. Lett.* **86**, 173501 (2005).

⁵E. Plis, J. B. Rodriguez, S. J. Lee, and S. Krishna, *Electron. Lett.* **42**, 1248 (2006).

⁶A. Gin, Y. Wei, A. Hood, A. Bajowala, V. Yazdanpanah, and M. Razeghi, *Appl. Phys. Lett.* **84**, 2037 (2004).

⁷S. Maimon and G. W. Wicks, *Appl. Phys. Lett.* **89**, 151109 (2006).

⁸J. B. Rodriguez, E. Plis, G. Bishop, Y. D. Sharma, H. Kim, L. R. Dawson, and S. Krishna, *Appl. Phys. Lett.* **91**, 043514 (2007).

⁹A. Khoshakhlagh, J. B. Rodriguez, E. Plis, G. D. Bishop, Y. D. Sharma, H. S. Kim, L. R. Dawson, and S. Krishna, *Appl. Phys. Lett.* **91**, 263504 (2007).

¹⁰G. Bishop, E. Plis, J. B. Rodriguez, Y. D. Sharma, H. S. Kim, L. R. Dawson, and S. Krishna, *J. Vac. Sci. Technol. B* **26**, 1 (2008).

¹¹E. Plis, S. Annamalai, K. T. Posani, S. Krishna, R. A. Rupani, and S. Ghosh, *J. Appl. Phys.* **100**, 014510 (2006).

¹²A. Hood, D. Hoffman, Y. Wei, F. Fuchs, and M. Razeghi, *Appl. Phys. Lett.* **88**, 052112 (2006).